arXiv:1512.02821v1 [astro-ph.EP] 9 Dec 2015

Temporary Capture of Asteroids by a Planet: Dependence of Prograde/Retrograde Capture on Asteroids' Semimajor Axes

A. Higuchi

Department of Earth and Planetary Sciences, Faculty of Science, Tokyo Institute of Technology, Meguro, Tokyo 152-8551, Japan

and

S. Ida

Earth-Life Science Institute, Tokyo Institute of Technology, Meguro, Tokyo 152-8550, Japan

Received _____; accepted _____

ABSTRACT

We have investigated the dependence of the prograde/retrograde temporary capture of asteroids by a planet on their original heliocentric semimajor axes through analytical arguments and numerical orbital integrations in order to discuss the origins of irregular satellites of giant planets. We found that capture is mostly retrograde for the asteroids near the planetary orbit and is prograde for those from further orbits. An analytical investigation reveals the intrinsic dynamics of these dependences and gives boundary semimajor axes for the change in prograde/retrograde capture. The numerical calculations support the idea of deriving the analytical formulae and confirm their dependence. Our numerical results show that the capture probability is much higher for bodies from the inner region than for outer ones. These results imply that retrograde irregular satellites of Jupiter are most likely to be captured bodies from the nearby orbits of Jupiter that may have the same origin as Trojan asteroids, while prograde irregular satellites originate from far inner regions such as the main-belt asteroid region.

Subject headings: planets and satellites: formation

1. Introduction

Irregular satellites around giant planets are small satellites with elliptical and inclined orbits (e.g., Jewitt & Haghighipour 2007; Nicolson et al. 2008). They have relatively large (planetocentric) semimajor axes. Because of their orbits, they are usually thought to be captured passing asteroids rather than formed *in situ*. In some cases, when the velocity of an asteroid relative to the planet is relatively low, it is temporarily trapped in the planetary Hill sphere. The trapped body must eventually exit the Hill sphere. But, if some energy loss (e.g., tidal dissipation, drag force from a circumplanetary disk when it existed, or collisions with other solid bodies in the disk) affects the asteroid's orbit, it can be permanently captured afterward. In fact, such temporary capture events have been observed. Examples include (1) comet D/Shoemaker-Levy 9, which impacted Jupiter (Weaver et al. 1995), (2) $2006RH_{120}$, which spent some time within Earth's Hill radius and was observed during the capture (e.g., Kwiatkowski et al. 2009), and (3) some bodies, including 147/Kushida-Muramatsu, which were found to be temporarily captured by Jupiter through backward orbital integrations (Ohtsuka et al. 2008).

Many studies on the origins of irregular satellites have been published (e.g., Kary & Dones 1996; Astakhov et al. 2003; Ćuk & Burns 2004; Nesvorný et al. 2007; Philpott et al. 2010; Suetsugu et al. 2011; Nesvorný et al. 2014). However, they mainly used numerical orbital integrations in the restricted three-body problem or more complex framework (e.g., with gas drag or perturbations from other objects), so it is not easy to understand general relationships between the original heliocentric orbits of the captured asteroids and their planetocentric orbits as satellites.

In this study, we approximate a circular three-body problem (Sun-planet-asteroid) into a combination of two independent two-body problems (Sun-asteroid and planet-satellite), identifying the asteroid with the satellite, and derive the relation between the pre-capture

heliocentric orbit and the planetocentric orbit at the moment of capture. We derive analytical formulae with simple assumptions and show that the formulae reproduce the results of orbital integrations very well. The analytical formulae reveal the intrinsic dynamics that regulates the relation between the heliocentric and planetocentric orbital elements. In particular, we show a clear dependence of prograde vs. retrograde capture of Jupiter's irregular satellites on the heliocentric semimajor axes of the original asteroids.

We describe the assumptions, basic formulation, derivation of the analytical formulae, and show orbital distributions generated by the formulae in Section 2. The methods and results of numerical calculations are presented in Section 3. In Section 4, we summarize the results and discuss the origin of Jupiter's irregular satellites, referring to results of the photometric observations.

2. Analytical Prediction for Temporary Capture

We first derive analytical formulae for temporary capture. Next, we generate the distribution of planetocentric orbits of the temporarily captured satellites using the formulae.

2.1. Derivation of Formulae for Temporary Capture

2.1.1. Assumptions

We use four conditions for temporary capture. We split a circular three-body problem (Sun-planet-asteroid) into two independent two-body problems (Sun-asteroid and planet-asteroid), identifying the asteroid with the satellite. We use the relative velocity between the asteroid and the planet in heliocentric orbits as a satellite velocity orbiting

around the planet (condition [1]) at the L_1 or L_2 Lagrangian point of the planet, which is a Hill radius away from the planet on the $x-$axis (condition [2]). The Hill radius is defined by $r_{\rm H} = a_{\rm p}(m_{\rm p}/3M_\odot)^{1/3}$, where $a_{\rm p}$ and $m_{\rm p}$ are the semimajor axis and mass of the planet and $M_\odot$ is the solar mass. Entering the zero-velocity surface that surrounds the planet via the L_1 or L_2 points provides the easiest access to planetocentric orbits in the restricted three-body problem (e.g., Murray & Dermott 1999).

Additionally, we set two other conditions to make the derivation simpler: we assume that the body's position at the moment of transition from heliocentric motion to planetocentric motion, (i.e., the L_1 or L_2 point) is the aphelion or perihelion of the heliocentric orbit (condition [3]). Condition [3], which implies that the relative radial velocity is zero, leads to the condition that the body has its apocenter or pericenter on the planetocentric orbit at L_1 or L_2 (condition [4]). An apocenter at L_1 or L_2 corresponds to a planetocentric orbit within $r_{\rm H}$ from the planet. A temporary capture does not always start with such a tightly bound orbit, so we relax the condition to having either an apocenter *or* pericenter at L_1 or L_2. Condition [4] is not always a good approximation because the planet's gravitational pull creates a velocity component radial to the planet. However, condition [3] is usually an acceptable approximation, so that condition [4] is necessary for the identification between heliocentric and planetocentric motions.

2.1.2. Conditions for Temporary Capture

We consider a body and a planet in the rotating Cartesian coordinates (x, y, z) centered on the Sun. The x-axis is chosen as parallel to the planet's position vector from the Sun and the x-y plane lies in the planet's orbital plane.

The heliocentric velocity of the body (an asteroid) at the heliocentric distance r is

$$v = \sqrt{GM_\odot \left(\frac{2}{r} - \frac{1}{a}\right)}, \tag{1}$$

where G is the gravitational constant, $M_\odot$ is the solar mass, and a is the heliocentric semimajor axis of the body. Using Equation (1) and conditions [2] and [3], we obtain the velocity at the orbit transition from heliocentric to planetocentric orbit as

$$v = \sqrt{GM_\odot \left(\frac{2}{A_\mp a_\mathrm{p}} - \frac{1}{a}\right)} = v_\mathrm{p}\chi, \tag{2}$$

$$\chi = \sqrt{\frac{2}{A_\mp} - \frac{a_\mathrm{p}}{a}}, \tag{3}$$

$$\begin{cases} A_- = 1 - \hat{r}_\mathrm{H} \ \text{ at } \ L_1 \\ A_+ = 1 + \hat{r}_\mathrm{H} \ \text{ at } \ L_2, \end{cases} \tag{4}$$

where $v_\mathrm{p} = \sqrt{GM_\odot/a_\mathrm{p}}$ and $\hat{r}_\mathrm{H} = r_\mathrm{H}/a_\mathrm{p}$.

From condition [3], the velocity vector is written as $(v_x, v_y, v_z) = (0, v\cos i, v\sin i)$, where i is the heliocentric orbital inclination of the body measured from the orbital plane of the planet. The planet has a heliocentric velocity $\mathbf{v}_\mathrm{p} = (0, v_\mathrm{p}, 0)$.

The velocity of the body (a satellite) orbiting around the planet is written as

$$v_\mathrm{s} = \sqrt{Gm_p \left(\frac{2}{r_\mathrm{s}} - \frac{1}{a_\mathrm{s}}\right)}, \tag{5}$$

where r_s and a_s are the planetocentric distance and semimajor axis of the body. From condition [4],

$$r_\mathrm{s} = a_\mathrm{s}\frac{1 - e_\mathrm{s}^2}{1 + e_\mathrm{s}\cos f_\mathrm{s}} = r_\mathrm{H}, \tag{6}$$

where e_s and f_s are the eccentricity (satellite eccentricity) and the true anomaly of the body in the planetocentric orbit.

Substituting Equation (6) into (5), we obtain

$$v_{\rm s} = v_{\rm p}\sqrt{\frac{m_{\rm p}}{M_\odot}\frac{\kappa}{\hat{r}_{\rm H}}} = \sqrt{3\kappa}v_{\rm p}\hat{r}_{\rm H}, \tag{7}$$

$$\kappa = \frac{1+e_{\rm s}^2+2e_{\rm s}\cos f_{\rm s}}{1+e_{\rm s}\cos f_{\rm s}}, \tag{8}$$

If condition [4] is satisfied, Equation (8) becomes a function only of $e_{\rm s}$,

$$\begin{cases} \kappa = 1-e_{\rm s} & \text{at planetocentric apocenter} \\ \kappa = 1+e_{\rm s} & \text{at planetocentric pericenter,} \end{cases} \tag{9}$$

and

$$r_{\rm s} = a_{\rm s}\frac{1-e_{\rm s}^2}{1+e_{\rm s}\cos f_{\rm s}} = r_{\rm H}, \tag{10}$$

where $f_{\rm s} = 0$ and $f_{\rm s} = 180^\circ$ are substituted at apocenter and pericenter, respectively. We use κ defined by Equation (9) as a parameter.

2.2. Heliocentric Orbital Elements for Temporary Capture -Planar Case

First, we consider the simplest planar case with $i = 0$ to understand how the orbital character (prograde or retrograde) is determined by the original heliocentric semimajor axis of a temporarily captured body. We will discuss general cases with non-zero i later. However, as we will show, for the body to be captured, the heliocentric orbital inclination must be relatively small ($i \lesssim 10^\circ$) so that the discussion of the planar case can be generalized to understand all other cases.

The capture would be prograde if $v_{\rm rel} = v_y - v_{\rm p} < 0$ at L_1 or $v_{\rm rel} > 0$ at L_2. Otherwise, the capture would be retrograde. From Equation (2),

$$v_{\rm rel} = v_{\rm p}\left(\chi - 1\right). \tag{11}$$

This equation implies that the capture is

$$\begin{cases} \text{prograde if } \dfrac{a}{a_{\rm p}} < B_- \quad \text{and} \quad \text{retrograde if } \dfrac{a}{a_{\rm p}} > B_- \quad [\text{at } L_1], \\ \text{retrograde if } \dfrac{a}{a_{\rm p}} < B_+ \quad \text{and} \quad \text{retrograde if } \dfrac{a}{a_{\rm p}} > B_+ \quad [\text{at } L_2], \end{cases} \tag{12}$$

where

$$B_- = \frac{1-\hat{r}_{\rm H}}{1+\hat{r}_{\rm H}} \text{ and } B_+ = \frac{1+\hat{r}_{\rm H}}{1-\hat{r}_{\rm H}}. \tag{13}$$

We always find that $B_- < 1 < B_+$ and the difference between B_- and B_+ is larger for bigger $m_{\rm p}$ (larger $\hat{r}_{\rm H}$).

If the relative velocity $|v_{\rm rel}|$ exceeds the velocity limit for bounded orbits around the planet, the body cannot be temporarily captured. As Equation (11) shows, $v_{\rm rel}$ takes a large negative value when a is too small (i.e., $\chi \to 0$) and a large positive value when a is too large (i.e., $\chi \to \sqrt{2/(1 \pm \hat{r}_{\rm H})}$). Thus, temporary capture is possible for bodies with heliocentric semimajor axes in some range encompassing $a_{\rm p}$. We will derive the range of a in the following.

During the transition from a heliocentric orbit to a planetocentric orbit, $v_{\rm rel} = \pm v_{\rm s}$ for some value of κ. For the body to have an orbit bounded to the planet, $e_{\rm s} < 1$, that is, $0 \le \kappa < 2$. Using Equations (7) and (11),

$$\chi - 1 = \mp (3\kappa)^{1/2} \hat{r}_{\rm H} \tag{14}$$

where $-$ and $+$ in the rhs correspond to $a < a_{\rm p}$ and $a > a_{\rm p}$, respectively, and are independent of $\mp$ in $A_{\mp}$. Using Equation (3), Equation (14) is rewritten as

$$\frac{a}{a_{\rm p}} = \left\{ \frac{2}{A_{\mp}} - \left[1 \mp (3\kappa)^{\frac{1}{2}} \hat{r}_{\rm H} \right]^2 \right\}^{-1}. \tag{15}$$

Thus, both the minimum and the maximum values of a are given with $\kappa = 2$:

$$\frac{a_{\min\mp}}{a_{\rm p}} = C_{\mp} = \left\{ \frac{2}{A_{\mp}} - \left[1 - \sqrt{6} \hat{r}_{\rm H} \right]^2 \right\}^{-1}, \tag{16}$$

$$\frac{a_{\max\mp}}{a_{\rm p}} \;=\; D_{\mp} \;=\; \left\{ \frac{2}{A_{\mp}} - \left[1 + \sqrt{6}\hat{r}_{\rm H}\right]^2 \right\}^{-1}, \tag{17}$$

where $-$ and $+$ correspond to expressions with $A_- = 1 - \hat{r}_{\rm H}$ and those with $A_+ = 1 + \hat{r}_{\rm H}$, respectively. Note that $C_- < C_+ < 1 < D_- < D_+$. Combining Equations (12), (16), and (17), we find that L_1 capture is

$$\begin{cases} \text{prograde for} \quad C_- < \dfrac{a}{a_{\rm p}} < B_-, \\ \text{retrograde for} \quad B_- < \dfrac{a}{a_{\rm p}} < D_-, \end{cases} \tag{18}$$

while L_2 capture is

$$\begin{cases} \text{retrograde for} \quad C_+ < \dfrac{a}{a_{\rm p}} < B_+, \\ \text{prograde for} \quad B_+ < \dfrac{a}{a_{\rm p}} < D_+. \end{cases} \tag{19}$$

In other words, the capture direction is summarized as

$$\begin{array}{lll} \text{(1) only prograde} & \text{for} & C_- < a/a_{\rm p} < C_+, \\ \text{(2) prograde via } L_1 \text{ and retrograde via } L_2 & \text{for} & C+ < a/a_{\rm p} < B_-, \\ \text{(3) only retrograde} & \text{for} & B_- < a/a_{\rm p} < B_+, \\ \text{(4) prograde via } L_2 \text{ and retrograde via } L_1 & \text{for} & B_+ < a/a_{\rm p} < D_-, \\ \text{(5) only prograde} & \text{for} & D_- < a/a_{\rm p} < D_+, \end{array} \tag{20}$$

where $B_\pm$ is defined by Equation (13) and $C_\mp$ and $D_\mp$ are defined by Equations (16) and (17), respectively. For example, for $m_{\rm p} = 9.55 \times 10^{-4} M_\odot$ and $a_{\rm p} = 5.2$ AU, $\hat{r}_{\rm H} = 0.068$ and $C_- a_{\rm p} = 3.6$ AU, $C_+ a_{\rm p} = 4.4$ AU, $B_- a_{\rm p} = 4.5$ AU, $B_+ a_{\rm p} = 6.0$ AU, $D_- a_{\rm p} = 6.6$ AU, and $D_+ a_{\rm p} = 10.2$ AU. Therefore, whether prograde or retrograde capture dominates clearly depends on the heliocentric semimajor axis of the captured body. The ratio of prograde capture to retrograde capture in the ranges of (2) and (4) is determined by the ratio of capture via L_1 to that via L_2, depending on the distributions of heliocentric orbital elements of asteroids.

2.3. Heliocentric Orbital Elements for Temporary Capture -General Case

2.3.1. Generalized Condition for Temporary Capture

Now we extend the discussions in section 2.2 to the general case by including inclined (asteroidal) orbits. The velocity at the orbit transition from a heliocentric to planetocentric orbit with heliocentric orbital inclination i is $(v_x, v_y, v_z) = (0, v_{\rm p}\chi\cos i, v_{\rm p}\chi\sin i)$. Then, the relative velocity of the body to the planet is written as

$$\begin{aligned} v_{\rm rel} &= \left(v_{{\rm rel},y}^2 + v_{{\rm rel},z}^2\right)^{\frac{1}{2}} \\ &= \left[(v_y - v_{\rm p})^2 + v_z^2\right]^{\frac{1}{2}} \\ &= v_{\rm p}\left[\chi^2 + 1 - 2\chi\cos i\right]^{\frac{1}{2}}. \end{aligned} \tag{21}$$

With $|v_{\rm rel}| = v_{\rm s}$, the equation of temporary capture can be written as follows:

$$\chi^2 - 2\chi\cos i + 1 - 3\kappa\hat{r}_{\rm H}^2 = 0. \tag{22}$$

Equation (22) connects the incoming heliocentric orbital elements before the capture (a, i) with the planetocentric orbital elements at the moment of capture ($a_{\rm s}$, $e_{\rm s}$, $i_{\rm s}$). Equation (22) also gives the range of these orbital parameters that satisfy the conditions of temporary capture by substituting $0 \leq \kappa < 2$. As already shown in Equation (9), κ is a parameter that shows the position along the planetocentric orbit at the moment of capture. The body captured at apocenter corresponds to $0 < \kappa < 1$, and to $1 < \kappa < 2$ when captured at pericenter. The planetocentric orbit of a body captured at pericenter has its apocenter at $\kappa r_{\rm H}$, which is outside the Hill radius. In general, temporary capture that results in a tightly bound orbit within planet's Hill radius corresponds to $0 \leq \kappa < 1$ rather than $1 \leq \kappa < 2$.

Range of the Semimajor Axis. The a range for temporary capture is given by solving Equation (22) and substituting Equation (3) into the solution. We use an $a_{\rm min}$ and $a_{\rm max}$ of

$$\frac{a_{\rm min\mp}}{a_{\rm p}} = \left\{ \frac{2}{A_{\mp}} - \left[\cos i - \sqrt{\cos^2 i - 1 + 6\hat{r}_{\rm H}^2} \right]^2 \right\}^{-1}, \tag{23}$$

$$\frac{a_{\rm max\mp}}{a_{\rm p}} = \left\{ \frac{2}{A_{\mp}} - \left[\cos i + \sqrt{\cos^2 i - 1 + 6\hat{r}_{\rm H}^2} \right]^2 \right\}^{-1}. \tag{24}$$

These are generalized forms of Equations (16) and (17). The values of $a_{\rm min}$ and $a_{\rm max}$ for $i = 0$ for eight planets are given in Table 1. Equations (23) and (24) show that the $a-$ range for temporary capture becomes largest when $i = 0$. This is because $v_{\rm rel}$ is smaller for smaller i and $a \sim a_{\rm p}$ (Eq. (21)). In other words, small i is required for a body with a far from the planet to be captured.

Range of Inclination. Figure 1 shows solutions to Equation (22) on the $a - i$ plane, for Jupiter with $a_{\rm p} = 5.2$AU and $m_{\rm p} = 9.55 \times 10^{-4} M_{\odot}$ for $0 \leq \kappa \leq 2$. For these planetary parameters, L_1 and L_2 are located at 4.84 and 5.56AU, respectively. The two feet of the curves in each panel touching the $x-$axis for $\kappa = 2$ correspond to $C_- a_{\rm p}$, $C_+ a_{\rm p}$, $D_- a_{\rm p}$, and $D_+ a_{\rm p}$. As shown in the derivation of Equations (23) and (24), $C_- a_{\rm p}$ and $D_+ a_{\rm p}$ are $a_{\rm min}$ and $a_{\rm max}$ for $i = 0$, respectively.

The region where a has a real value in Equation (22) is defined by the region enclosed with the curve for $\kappa = 2$ and the x-axis in Figure 1. Hereafter, we call this region as the TC region.

The maximum inclination in the TC region is given by

$$i_{\rm max} = \arccos\left(\sqrt{1 - 6\hat{r}_{\rm H}^2} \right), \tag{25}$$

This is a function only of the mass of the planet. For $m_{\rm p} = 9.55 \times 10^{-4} M_{\odot}$, $i_{\rm max} \simeq 9.6°$. The values of $i_{\rm max}$ for the eight planets are listed in Table 1.

Range of the Tisserand Parameter. Figure 2 shows the TC region on the $a - T$ plane where T is the Tisserand parameter defined as

$$T = \frac{a_{\rm p}}{a} + 2\sqrt{\frac{a}{a_{\rm p}}(1-e^2)}\cos i. \tag{26}$$

The Tissserand parameter shows the orbital relation between the body and the planet in the circular restricted three-body framework: bodies with $T > 3$ never cross the planetary orbit. So the existence of the TC regions for $T > 3$ means that planets can capture bodies whose orbits are not potentially planetary orbit-crossing. The minimum and maximum values of T for the eight planets are numerically computed and given in Table 1.

2.3.2. Satellite inclination

The instantaneous inclination of the planetocentric orbits ("satellite inclination") is computed from the angular momentum. The satellite's angular momentum at the L_1 or L_2 points $\mathbf{r}_{\rm s} = (r_{\rm s}, 0, 0)$ with the velocity $\mathbf{v}_{\rm s} = (v_{{\rm s},x}, v_{{\rm s},y}, v_{{\rm s},z})$ is written as

$$\begin{aligned}
\mathbf{h}_{\rm s} &= \mathbf{r}_{\rm s} \times \mathbf{v}_{\rm s} \\
&= \begin{pmatrix} 0 \\ -r_{\rm s} v_{{\rm s},z} \\ r_{\rm s} v_{{\rm s},y} \end{pmatrix} \\
&= h_{\rm s} \begin{pmatrix} \sin\Omega_{\rm s} \sin i_{\rm s} \\ -\cos\Omega_{\rm s} \sin i_{\rm s} \\ \cos i_{\rm s} \end{pmatrix},
\end{aligned} \tag{27}$$

where the subscripts x, y, z denote the x, y, z components and $\Omega_{\rm s}$ is the longitude of the ascending node such that $\cos\Omega_{\rm s} = -1$ and 0 for L_1 and L_2 captures, respectively. Then,

$$\tan i_{\rm s} = \begin{cases} \frac{-v_{{\rm s},z}}{v_{{\rm s},y}} & \text{for } L_1 \text{ capture,} \\ \frac{v_{{\rm s},z}}{v_{{\rm s},y}} & \text{for } L_2 \text{ capture.} \end{cases} \tag{28}$$

Substituting $\mathbf{v}_{\rm s} = \mathbf{v}_{\rm rel}$ into Equation (28), we have

$$\tan i_{\rm s} = \begin{cases} \frac{\chi \sin i}{1-\chi\cos i} & \text{for } L_1 \text{ capture,} \\ \frac{\chi \sin i}{\chi\cos i - 1} & \text{for } L_2 \text{ capture.} \end{cases} \tag{29}$$

As already shown, the heliocentric i of the captured bodies is limited to $\lesssim 10^\circ$. However, note that Equation (29) shows that the planetocentric $i_{\rm s}$ can take any value. Figure 3 shows $i_{\rm s}$ as a function of a for various $i < i_{\rm max}$. The region between the two crosses on each curve is for capture at apocenter (i.e., $\kappa = 1 - e_{\rm s} < 1$).

The transition between prograde and retrograde captures occurs at $i_{\rm s} = 90^\circ$. From Equation (29), the heliocentric semimajor axis for this transition, a_{90}, is derived by $\chi = 1/\cos i$, that is,

$$\frac{a_{90}}{a_{\rm p}} = \left(\frac{2}{A_\pm} - \frac{1}{\cos^2 i} \right)^{-1}. \tag{30}$$

In the limit that $i \to 0$, this condition is reduced to $a/a_{\rm p} \to B_\mp$. The values of a_{90} for $i = 0$ for the eight planets are presented in Table 1 with $a_{\rm min}$ and $a_{\rm max}$ for $i = 0$. As already shown, another planetocentric orbital element, $e_{\rm s}$, is determined by $a_{\rm s}(1 \pm e_{\rm s}) = r_{\rm H}$ (Eq. (6)).

2.4. The Satellite's Inclination Distribution

Using Equations (22) and (29), we generate the planetocentric orbital distributions of satellites for Jupiter, $m_{\rm p} = 9.55 \times 10^{-4} M_\odot$ and $a_{\rm p} = 5.2$AU, assuming that the heliocentric $a - i$ distribution is uniform in the ranges $a_{\rm min} < a < a_{\rm max}$ and $i < i_{\rm max}$. We compute the distributions for L_1 and L_2 captures and add them.

The top panel in Figure 4 shows the $i_{\rm s}$ distribution for various ranges of the heliocentric semimajor axis a. The vertical axis indicates the fraction of bodies in each a bin with

a width of 0.5 AU. Basically, the behavior is similar to the relation in the case $i = 0$ summarized in Equation (20); for the middle a range near $a_{\rm p}$ (i.e., $4.2 < a < 6.2$ AU), the distribution is dominated by retrograde orbits, whereas the a range on both sides of it (i.e., $a < 4.2$ AU and $a > 6.2$) is dominated by prograde orbits. The peak of the $i_{\rm s}-$ distribution shifts outward as a function of a for $a < 5.2$ AU and inward for $a > 5.2$ AU. The lowest values of $i_{\rm s}$ are obtained for a farthest from $a = 5.2$ AU; this can be explained by the small i allowed for the capture as shown in Equations (23) and (24) and Figure 1. With small i, the orbital behavior around these regions is similar to that of the coplanar case i.e., $i_{\rm s}$ is close to 0 or 180°. The distribution of some a regions that satisfy the temporary capture condition at both L_1 and L_2 has a secondary peak.

Note that the top panel of Figure 4 is generated using the assumption that L_1 and L_2 captures occur with the same probability and that κ uniformly ranges from 0 to 2. If we consider temporary capture as the origin of irregular satellites, orbits with $\kappa < 1$ should be more favorable because orbits with $\kappa < 1$ correspond to tightly bound orbits and those with $\kappa > 1$ correspond to elongated satellite orbits with their apocenter outside the Hill sphere of the planet. The numerical calculations in the next section clearly show this trend.

3. Comparison with Numerical Results

We perform numerical calculations for temporary capture of bodies by Jupiter to evaluate the relevance of our analytical formulae. We will show that the dependence of prograde/retrograde capture on the heliocentric semimajor axis of asteroids predicted by our formulae agrees with the numerical results.

3.1. Methods and Initial Conditions

We compute the orbital evolution of 5×10^4 bodies perturbed by Jupiter moving along a circular orbit, using a 4th order Hermite integration scheme for 10^6 years or less. In our analytical derivation (Section 2), the three-body problem was split into two problems of two bodies, Sun-asteroid and Jupiter-asteroid. Here, because we use numerical orbital integration, we consider the circular restricted three-body problem (Sun-Jupiter-asteroid), just as previous investigators have (see the Introduction).

We consider asteroids to initially be uniformly distributed on the $a - T$ plane between $a_{\rm min} < a < a_{\rm max}$ and $T_{\rm min} < T < T_{\rm max}$. We randomly choose $i < i_{\rm max}$. The minimum and maximum values of a, T, and i and Jupiter's semimajor axis and mass used in the calculation are given in Table 1.

We count asteroids as temporary captures if they satisfy two conditions: (1) they must stay within 3 $r_{\rm H}$ from Jupiter longer than one orbital period of Jupiter and (2) the minimum distance from Jupiter be less than 1 $r_{\rm H}$. If an asteroid collides with Jupiter or the Sun, or has $e > 1$ at $r > 30$ AU, it is removed from the calculation. We output the heliocentric orbital elements of the temporarily captured asteroids at 3 $r_{\rm H}$ away from Jupiter before and then after the temporary capture. We also output the planetocentric orbital elements when 1 $r_{\rm H}$ away from Jupiter before and after the temporary capture. All the planetocentric orbital elements are calculated within a two-body framework that consists of Jupiter and the asteroids.

3.2. Results

3.2.1. Incident parameters to the Hill sphere

We have found 1.6×10^4 temporary captures by Jupiter during the calculation. Figure 5 shows the two-dimensional (2D) distribution of the positions of the captured bodies as they enter Jupiter's Hill sphere for the first time during each temporary capture. The two concentrations at $(x_{\rm s}, y_{\rm s}) = (-1, 0)$ and $(1, 0)$ correspond to L_1 and L_2, showing that condition [2] is approximately valid. The concentration around the perimeter is a geometrical effect. Condition [1] corresponds to $|v_{{\rm s},x}|, |v_{{\rm s},y}| < v_{\rm sat}$. Figure 6 show the 2D distribution of the incident velocities of the captured bodies on the $v_{{\rm s},x} - v_{{\rm s},y}$ plane at the same moment as Figure 5. The values of $v_{{\rm s},x}$ and $v_{{\rm s},y}$ are scaled by by the circular velocity of the satellite at $1r_{\rm H}$ away from Jupiter, $v_{\rm s0} = \sqrt{Gm_{\rm J}/r_{\rm H}}$, where $m_{\rm J}$ is Jupiter's mass. Since $|v_{{\rm s},x}|, |v_{{\rm s},y}| < v_{\rm s0}$ is mostly satisfied, condition [1] is approximately valid. The upper-left and lower-right peaks in Figure 6 correspond to the two concentrations at $(x_{\rm s}, y_{\rm s}) = (1, 0)$ and $(-1, 0)$ in Figure 5, which are at L_2 and L_1, respectively. Condition [3] corresponds to $|v_{{\rm s},x}| \gg |v_{{\rm s},y}|$, while the numerical orbital integrations show that $|v_{{\rm s},x}| \sim |v_{{\rm s},y}|$. The three-body effect, which we do not take into account, is important near $r_{\rm s} = r_{\rm H}$ and planet's gravitational pull to heliocentric orbits causes a non-zero value of $|v_{{\rm s},x}|$. Since $|v_{{\rm s},x}|$ is not larger than $|v_{{\rm s},y}|$, condition [4] would not be invalid. Figure 7 shows the distribution of the mean anomaly M and eccentricity in the heliocentric distance at the same moment for Figure 5. The two concentrations around $M \lesssim 0$ and $M \lesssim 180^\circ$ correspond to the aphelion and perihelion, showing that condition [3] is approximately valid. These concentrations are not found for small e, since the radial velocity is small even in the orbital phases far from apocenter and pericenter.

3.2.2. Distributions of planetocentric inclinations

The lower panel in Figure 4 shows the $i_{\rm s}$ distribution of the captured bodies when they cross the Jovian Hill sphere for the first time during each temporary capture (the same timing as Figure 5), as a function of the heliocentric semimajor axes just before (3 $r_{\rm H}$ away from Jupiter) the temporary capture ($a_{\rm tc}$). The distribution is scaled for individual $a_{\rm tc}$ bins. The relative frequency distribution among different $a_{\rm tc}$ is described in the next section.

The peaks of the distribution are shifted depending on $a_{\rm tc}$. The $a_{\rm tc}$ dependence is similar to the distribution generated in Section 2.4 using Equations (22), (28), and (29). The results of the numerical calculations share the following common features with the analytical predictions (the upper panel of Fig. 4), (1) Bodies originating from heliocentric semimajor axes at 4.7 AU $< a_{\rm tc} <$ 5.7 AU around Jupiter's orbit generally produce retrograde satellite orbits with the highest values of $i_{\rm s}$ when they are captured, and (2) Prograde orbiters with small $i_{\rm s} < 30^\circ$ mostly come from the regions relatively far from Jupiter's orbit, $a_{\rm tc} <$ 4.2 AU or $a_{\rm tc} >$ 8.2 AU. These features are also present in the results of the planar case in section 2.2, so that the basic dynamics for these are explained in section 2.2.

On the other hand, the analytical distribution (the upper panel of Figure 4) differs from our numerical results in the following ways: (1) The secondary peaks of 4.2 AU$< a_{\rm tc} <$6.7 AU at $i_{\rm s} \gtrsim 150^\circ$ in the analytical distribution are not found in the numerical distribution, while (2) the distributions for $a_{\rm tc} <$ 4.2 AU and $a_{\rm tc} >$ 6.7 AU are bimodal in the numerical distribution, but this was not predicted analytically. The peaks in (1) correspond to bodies captured at pericenter. As we anticipated in section 2.3, temporary captures at the pericenters of satellite orbits are infrequent, although such captures do exist. This feature is enhanced when we investigate longer temporary captures (e.g., $>$ 100 years). The bimodal distribution in (2) is probably due to differences between a in Equation (22)

and the numerically obtained $a_{\rm tc}$, caused by the assumption of splitting the restricted three-body problem into a pair of independent two-body problems that we have adopted to derive Equation (22).

3.2.3. Capture frequency as a function of the heliocentric semimajor axes of asteroids

The relative frequency distribution among different $a_{\rm tc}$ obtained by the numerical orbital integration is shown by the black histograms in Figure 8. In section 2.2, we predicted that temporary capture occurs only for asteroids between 3.6 AU $< a <$ 10.2 AU. The numerical result is consistent with this prediction. However, the distribution is strongly skewed toward smaller a within the region capable of capture, although we spread the initial heliocentric semimajor axes of asteroids uniformly.

The peak at relatively small a (4.2 AU $< a_{\rm tc} <$ 4.7 AU) may be due to the short orbital periods of the inner orbits and some stable regions in mean-motion resonances with Jupiter such as the 3:2 Hilda asteroids. This region corresponds to the $a_{\rm tc}$ bin producing the peak at $i_{\rm s} \simeq 110^\circ$. This may explain why giant planets have retrograde irregular satellites more often than prograde ones. The frequency for $a_{\rm tc} <$ 4.2 AU is much larger than that for $a_{\rm tc} >$ 7.7 AU. This means that the prograde orbiters with small $i_{\rm s} < 30^\circ$ are mainly from the inner region.

The orange and blue histograms in Figure 8 show the results of additional numerical calculations with an eccentric Jupiter ($e = 0.05$) instead of a circular Jupiter and with an extra perturbation from Saturn ($a_{\rm p} = 9.55$ AU, $m_{\rm p} = 2.86 \times 10^{-4} M_\odot$; cf. Kary & Dones (1996)). Neither the Jupiter's eccentricity nor Saturn's presence changes the overall features of the $a_{\rm tc}$ frequency distribution.

4. Summary and Discussion

To discuss the temporary capture of asteroids by a planet, we have investigated the dependence of prograde/retrograde (inclinations of the resultant satellite orbits) capture of asteroids on their original heliocentric semimajor axes using analytical arguments and numerical orbital integrations. In the orbital integrations, we solved the circular restricted three-body problem (Sun-Jupiter-asteroid). In the analytical arguments, we split the three-body problem into two independent systems of two-body problems (Sun-asteroid and planet-satellite), where the planetary semimajor axis and mass are scaled and the arguments are not specific to Jupiter. The two systems are combined by identifying the relative velocity between Jupiter's heliocentric circular orbit and the asteroid's heliocentric Keplerian eccentric orbit with a planetocentric Keplerian eccentric orbit as a satellite at the L_1 or L_2 points of the planet's Hill sphere.

We have found a clear dependence of prograde/retrograde capture on the pre-capture heliocentric semimajor axes of the asteroids. Capture is mostly retrograde for the asteroids from orbits near the planetary orbit, more specifically, from heliocentric semimajor axes a in the range

$$\frac{1-\hat{r}_{\rm H}}{1+\hat{r}_{\rm H}} \lesssim \frac{a}{a_{\rm p}} \lesssim \frac{1+\hat{r}_{\rm H}}{1-\hat{r}_{\rm H}}, \tag{31}$$

where $a_{\rm p}$ is the planet's semimajor axis, $\hat{r}_{\rm H} = (m_{\rm p}/3M_\odot)^{1/3}$, and $m_{\rm p}$ is the planetary mass. On the other hand, capture is mostly prograde for those asteroids from orbits far from the planetary orbit,

$$\frac{a}{a_{\rm p}} \lesssim \left\{ \frac{2}{1+\hat{r}_{\rm H}} - \left[1-\sqrt{6}\hat{r}_{\rm H}\right]^2 \right\}^{-1} \text{ or } \frac{a}{a_{\rm p}} \gtrsim \left\{ \frac{2}{1-\hat{r}_{\rm H}} - \left[1+\sqrt{6}\hat{r}_{\rm H}\right]^2 \right\}^{-1}. \tag{32}$$

We also found that asteroids at $a/a_{\rm p} \lesssim \left\{ \frac{2}{1-\hat{r}_{\rm H}} - \left[1-\sqrt{6}\hat{r}_{\rm H}\right]^2 \right\}^{-1}$ and $a/a_{\rm p} \gtrsim \left\{ \frac{2}{1+\hat{r}_{\rm H}} - \left[1+\sqrt{6}\hat{r}_{\rm H}\right]^2 \right\}^{-1}$ or those with heliocentric orbital inclinations larger than 10 degrees cannot be captured. The conditions (31) and (32) are come from the ana-

lytical arguments. The numerical orbital integrations show similar results, although the prograde/retrograde boundaries are less clear.

Our results indicate that retrograde irregular satellites are most likely to be captured bodies from the orbits near the host planet's orbit, whereas most prograde irregular satellites originate from farther regions on either side of the host planet. Note that our numerical results show that the capture probability is much higher for bodies from inner regions than for outer ones. Therefore, the prograde region is actually more concentrated than the retrograde region.

These results suggest that, in Jupiter's case, the retrograde irregular satellites likely originated as Trojan asteroids and the majority of the prograde irregular satellites are from far inner regions such as main-belt asteroids. This is consistent with the recent observations of irregular satellites and Trojan asteroids of Jupiter. Sykes et al. (2000) found differences between prograde and retrograde groups from near-infrared observations of six of the eight known Jovian irregular satellites detected in the Two-micron All Sky Survey. They suggested that the retrograde satellites exhibit much greater diversity among themselves than the prograde satellites and that the retrograde (prograde) satellites may be similar to D-type (C-type) asteroids, although their samples are only of eight objects. BVR photometry of Jovian irregular satellites presented by Rettig et al. (2001) and Grav et al. (2003) shows a concentration of prograde satellites in a small region, except Themisto, and a redder and more diverse distribution for retrograde satellites on the $B-V$ versus $V-R$ color-color plot. The region of the diversity of retrograde satellites matches that of Trojan asteroids given in Hainaut et al. (2012).

Small eccentricity ($e = 0.05$) for Jupiter made little difference in the results with a circular Jupiter case (Fig. 8). However, the effect of eccentricity, especially for less massive planets such as Mars, is not negligible. In our next paper we will expand the results to

eccentric planet cases.

We thank Takayuki Tanigawa for valuable discussions. We also thank an anonymous referee for his/her useful comments that helped to improve the paper. This work was supported by JSPS KAKENHI grant Number 23740335. Data analyses were in part carried out on the PC cluster at the Center for Computational Astrophysics, National Astronomical Observatory of Japan.

REFERENCES

Astakhov, S. A., Burbanks, A. D., Wiggins, S. & Farrelly, D. 2003, Nature, 423, 264

Ćuk, M. & Burns, J. A., 2004, Icarus, 167, 369

Grav, T., Holman, M. J., Gladman, B. J. & Aksnes, K. 2003, Icarus, 166, 33

Hainaut, O. R., Boehnhardt, H. & Protopapa, S. 2012, A&A, 546, A115

Jewitt, D & Haghighipour, N. 2007, ARA&A, 45, 261

Kary, D. M. & Dones, L. 1996, Icarus, 121, 207

Kwiatkowski, T., Kryszczyńska, A., Polińska, M., Buckley, D. A. H., O'Donoghue, D., Charles, P. A., Crause, L., Crawford, S., Hashimoto, Y., Kniazev, A., Loaring, N., Romeo Colmenero, E., Sefako, R., Still, M. & Vaisanen, P. A&A, 495, 967

Murray, C. D.& Dermott, S. F. 1999, Solar System Dynamics, Cambridge: Cambridge University Press

Nesvorný, D., Vokrouhlický, D., & Morbidelli, A. 2007, AJ, 133, 1962

Nesvorný, D., Vokrouhlický, D., & Deienno, R. 2014, ApJ, 784, 6

Nicolson, P. D., Ćuk, M., Sheppard, S. S., Nesvorný, D., & Johonson, T. V. 2008, in The Solar System Beyond Neptune, ed. M. A. Barucci et al. (Tucson, AZ: Univ. Arizona Press), 411

Ohtsuka, K., Ito, T., Yoshikawa, M., Asher, D. J. & Arakida, H. 2008, A&A, 489, 1355

Rettig, T. W., Walsh, K. & Consolmagno, G. 2001, Icarus, 154, 313

Philpott, C. M., Hamilton, D. P., & Agnor, C. B. 2010, Icarus, 208, 824

Suetsugu, R., Ohtsuki, K. & Tanigawa, T 2011, AJ, 142, 11

Sykes, M. V., Nelson, B., Cutri, R. M., Kirkpatrick, D. J. Hurt, R. & Skrutskie, M. F. 2000, Icarus, 143, 371

Weaver, H. A., A'Hearn, M. F., Arpigny, C., Boice, D. C., Feldman, P. D., Larson, S. M., Lamy, P., Levy, D. H., Marsden, B. G., Meech, K. J., Noll, K. S., Scotti, J. V., Sekanina, Z., Shoemaker, C. S., Shoemaker, E. M., Smith, T. E., Stern, S. A., Storrs, A. D., Trauger, J. T., Yeomans, D. K. & Zellner, B. Science, 267, 1282

This manuscript was prepared with the AAS LaTeX macros v5.2.

Planet	$a_{\rm p}$ (AU)	$m_{\rm p}$ ($M_\odot$)	$i_{\rm max}$ (degree)	L_1/L_2	$a_{\rm min}$ (AU)	a_{90} (AU)	$a_{\rm max}$ (AU)	$T_{\rm min}$	$T_{\rm max}$
Mercury	0.387	1.66e-07	0.5348	L_1	0.3771	0.384062	0.3913	2.99987	3.00004
				L_2	0.3828	0.389961	0.3975	2.99987	3.00004
Venus	0.723	2.45e-06	1.312	L_1	0.6794	0.709609	0.7434	2.99922	3.00026
				L_2	0.7042	0.736644	0.7731	2.99922	3.00026
Earth	1	3.00e-06	1.404	L_1	0.9358	0.980198	1.03	2.99911	3.0003
				L_2	0.9722	1.0202	1.075	2.99911	3.0003
Mars	1.52	3.72e-07	0.6999	L_1	1.47	1.50492	1.542	2.99978	3.00007
				L_2	1.498	1.53524	1.574	2.99978	3.00007
Jupiter	5.2	9.55e-04	9.628	L_1	3.579	4.53527	6.632	2.95919	3.01467
				L_2	4.412	5.96215	10.2	2.95792	3.01339
Saturn	9.55	2.86e-04	6.425	L_1	7.307	8.71559	11.11	2.98163	3.00646
				L_2	8.497	10.4643	14.12	2.98125	3.00608
Uranus	19.2	4.37e-05	3.43	L_1	16.46	18.2845	20.72	2.99472	3.00182
				L_2	17.97	20.1613	23.16	2.99466	3.00176
Neptune	30.1	5.15e-05	3.623	L_1	25.61	28.5861	32.63	2.99411	3.00203
				L_2	28.08	31.6941	36.74	2.99404	3.00196

Table 1: Ranges of i, a, and T from Equation (22) and a_{90} from Equation (30) for eight planets.

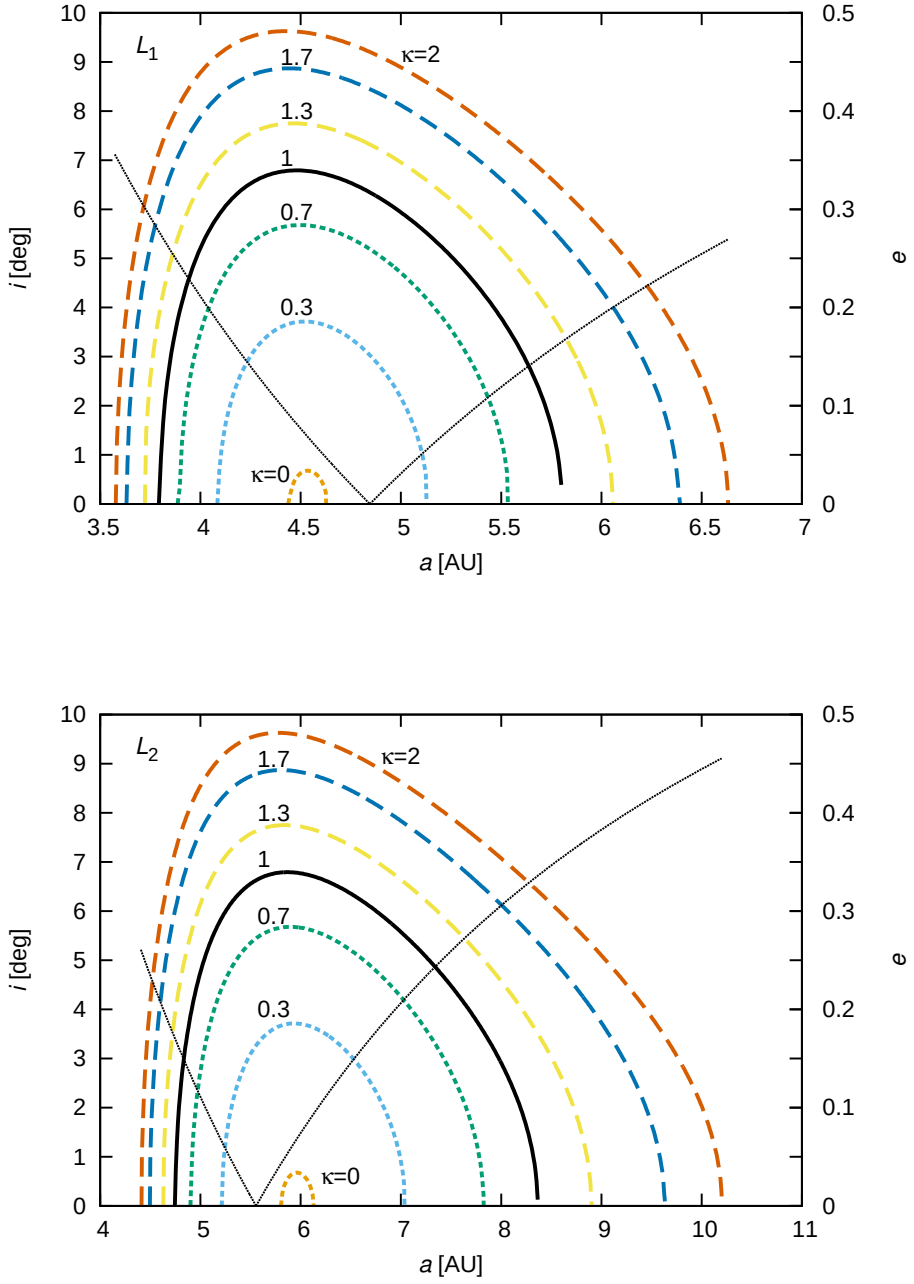

Fig. 1.— Solutions to Equation (22) on the $a - i$ plane for various κ. The upper and lower panels are for L_1 and L_2 capture, respectively. The numbers labeled on the curves represent the values of κ. The eccentricity e given for each a by condition [3] is also plotted against the secondary (right) $y-$axis (thin dashed curve). The upper and lower panels are for L_1 and L_2 capture, respectively.

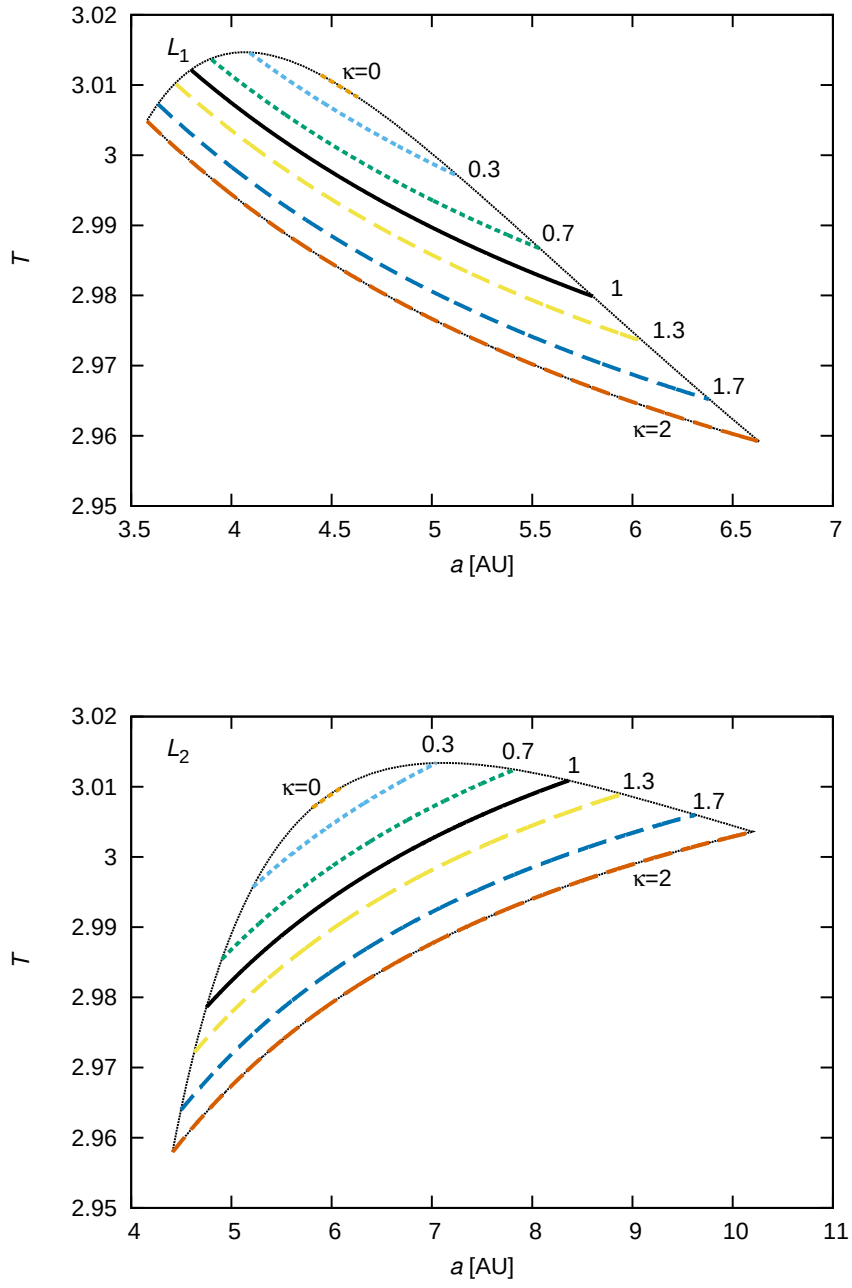

Fig. 2.— Solutions to Equation (22) on the $a - T$ plane for various κ. The upper and lower panels are for L_1 and L_2 capture, respectively. The numbers labeled on the curves represent the values of κ. The black envelope shows the TC regions filled with curves for $0 < \kappa < 2$.

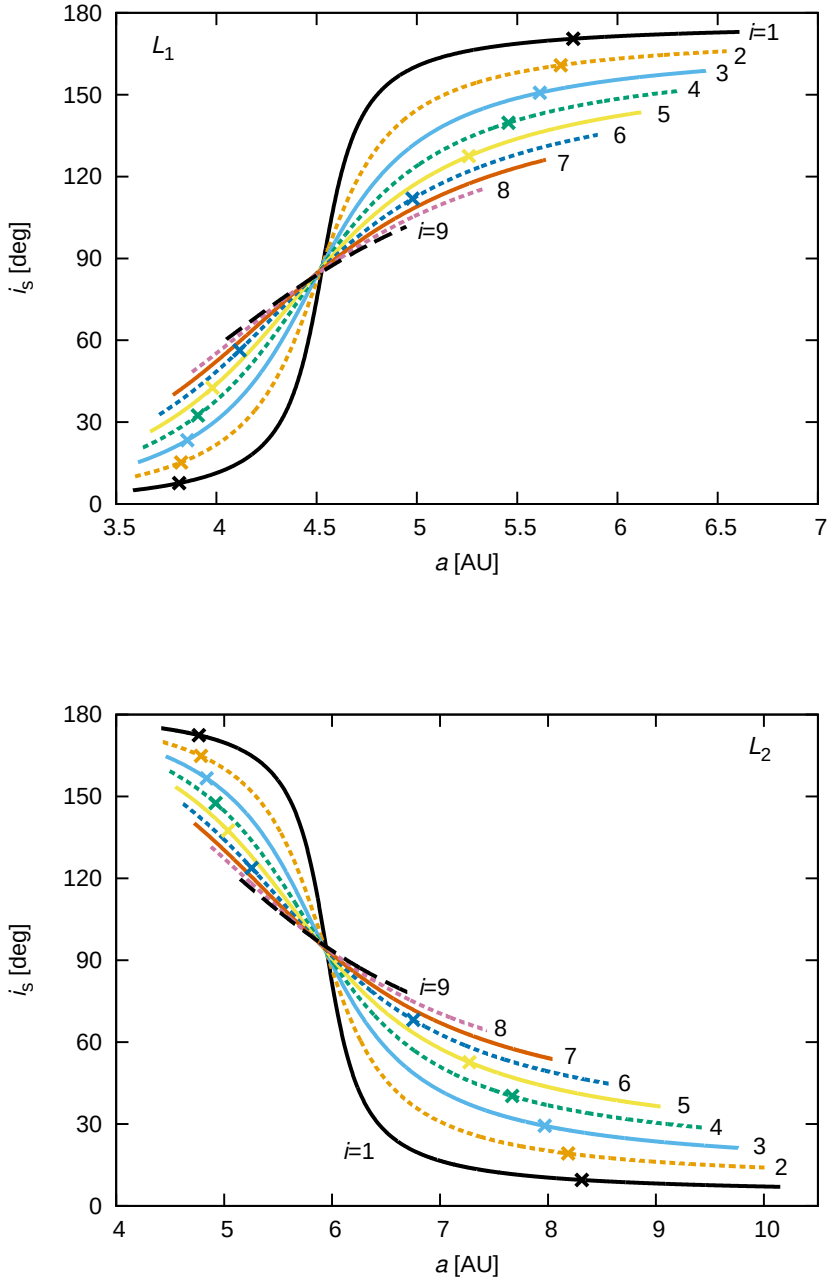

Fig. 3.— Satellite inclination i_s of the planetocentric orbits as a function of heliocentric semimajor axis a for various heliocentric inclinations i, given by Equation (29). The upper and lower panels are for L_1 and L_2 capture, respectively. The numbers labeled on the curves represent the values of i. Two crosses in each curve show the points of $\kappa = 1$ capture. The solutions between the two crosses on each curve correspond to $\kappa < 1$ capture.

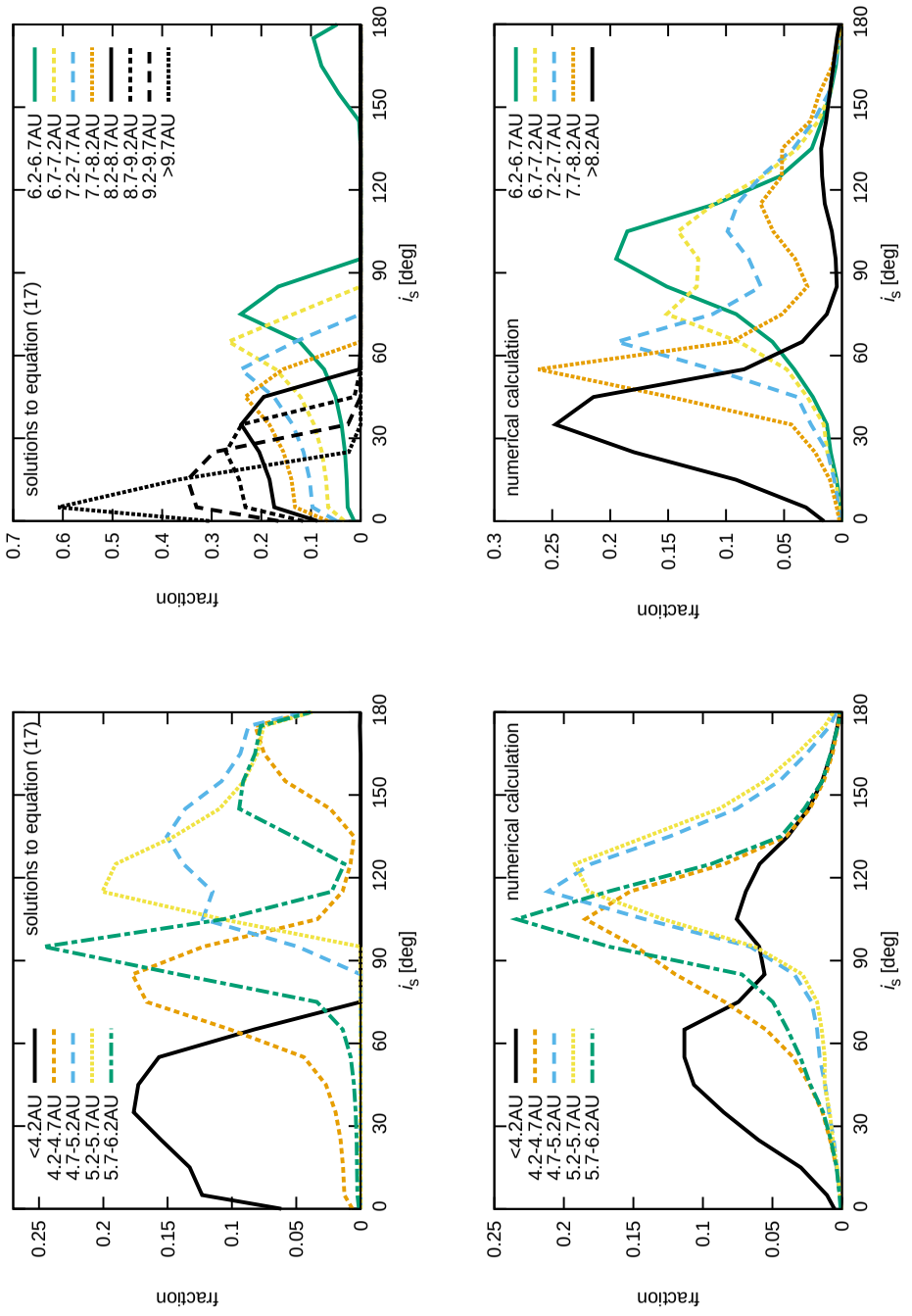

Fig. 4.— Distribution of satellite orbital inclination i_s obtained from Eqs. (22) and (29) assuming a uniform distribution on the $a - i$ plane for various a (upper panels), compared with results from numerical calculation (lower panels).

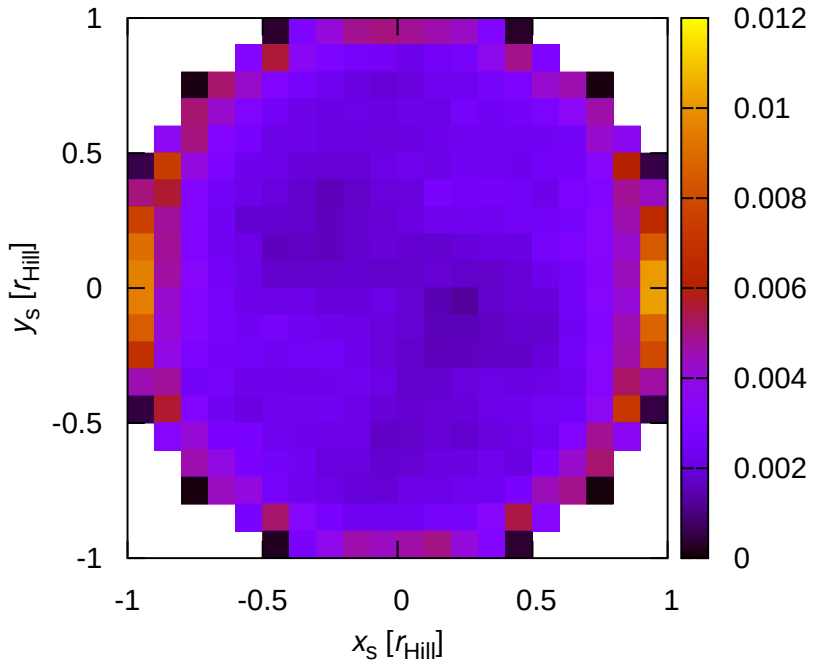

Fig. 5.— Location of the bodies on the Hill sphere of Jupiter on the $x_s - y_s$ plane, at the moment when the bodies enter the Hill sphere for the first time during each temporary capture.

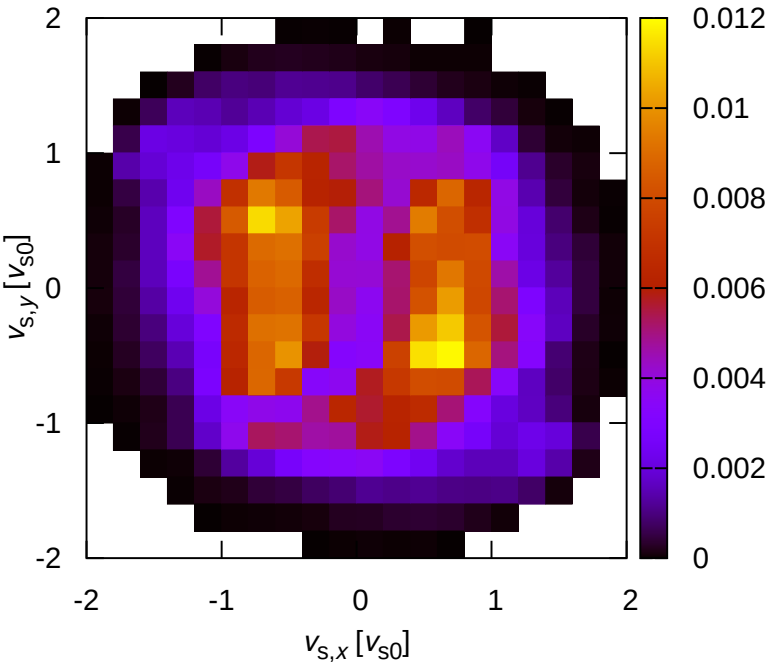

Fig. 6.— Velocity distribution of the bodies on the Hill sphere of Jupiter on the $v_{s,x} - v_{s,y}$ plane, at the moment when the bodies enter the Hill sphere for the first time during each temporary capture. The values are scaled by the circular veocity of the satellite at $1r_H$ away from Jupiter.

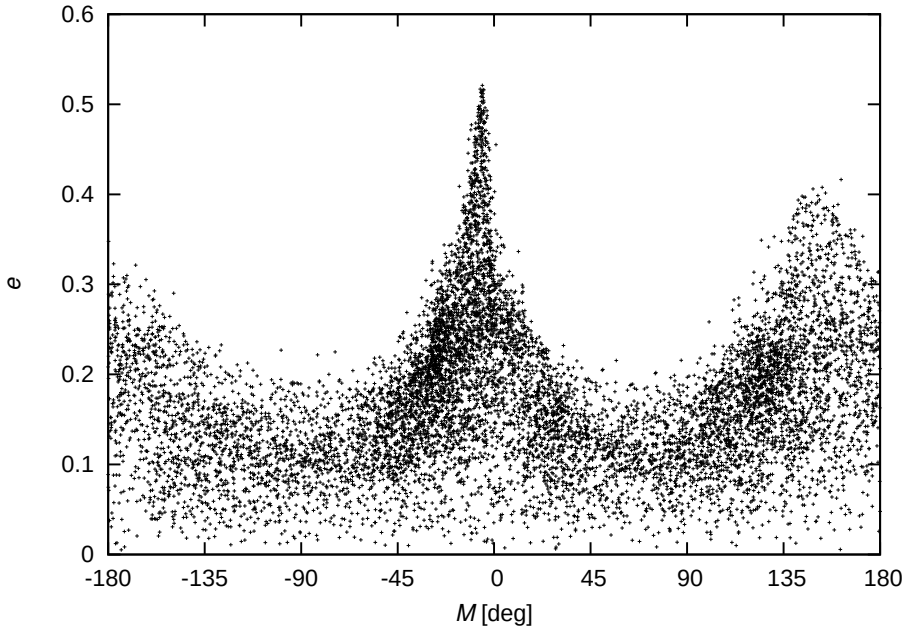

Fig. 7.— Distribution of the mean anomaly M and eccentricity of the bodies in heliocentric orbit, at the moment when the bodies enter the Hill sphere for the first time during each temporary capture (the same as Fig. 5).

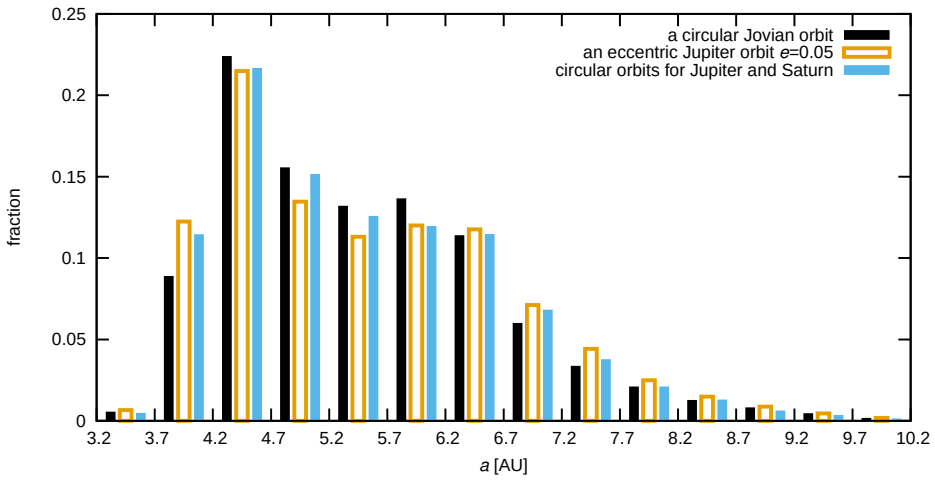

Fig. 8.— Distribution of $a_{\rm tc}$ obtained by numerical calculations. Black: with a circular Jovian orbit; open orange: with an eccentric Jupiter orbit ($e = 0.05$, additional calculations); blue: with circular orbits for Jupiter and Saturn (additional calculations).